PHYSICAL REVIEW SPECIAL TOPICS - ACCELERATORS AND BEAMS **12**, 080705 (2009)

Transient self-amplified Cerenkov radiation with a short pulse electron beam

B. R. Poole[*] and D. T. Blackfield[†]
Lawrence Livermore National Laboratory, Livermore, California 94551, USA

J. F. Camacho[‡]
NumerEx LLC, Albuquerque, New Mexico 87106, USA
(Received 9 February 2009; published 24 August 2009)

An analytic and numerical examination of the slow wave Cerenkov free electron maser is presented. We consider the steady-state amplifier configuration as well as operation in the self-amplified spontaneous emission (SASE) regime. The linear theory is extended to include electron beams that have a parabolic radial density inhomogeneity. Closed form solutions for the dispersion relation and modal structure of the electromagnetic field are determined in this inhomogeneous case. To determine the steady-state response, a macroparticle approach is used to develop a set of coupled nonlinear ordinary differential equations for the amplitude and phase of the electromagnetic wave, which are solved in conjunction with the particle dynamical equations to determine the response when the system is driven as an amplifier with a time harmonic source. We then consider the case in which a fast rise time electron beam is injected into a dielectric loaded waveguide. In this case, radiation is generated by SASE, with the instability seeded by the leading edge of the electron beam. A pulse of radiation is produced, slipping behind the leading edge of the beam due to the disparity between the group velocity of the radiation and the beam velocity. Short pulses of microwave radiation are generated in the SASE regime and are investigated using particle-in-cell (PIC) simulations. The nonlinear dynamics are significantly more complicated in the transient SASE regime when compared with the steady-state amplifier model due to the slippage of the radiation with respect to the beam. As strong self-bunching of the electron beam develops due to SASE, short pulses of superradiant emission develop with peak powers significantly larger than the predicted saturated power based on the steady-state amplifier model. As these superradiant pulses grow, their pulse length decreases and forms a series of solitonlike pulses. Comparisons between the linear theory, macroparticle model, and PIC simulations are made in the appropriate regimes.

DOI: 10.1103/PhysRevSTAB.12.080705 PACS numbers: 41.60.Bq, 41.60.Cr

I. INTRODUCTION

It is well known that the passage of an electron beam through a slow wave structure can be used either to amplify or generate electromagnetic radiation. The general mechanism for microwave generation by the Cerenkov effect is the interaction of the slow space-charge wave on an electron beam with the normal modes of a dielectric lined waveguide. The interaction is strongest when the beam velocity is synchronous with the phase velocity of the electromagnetic wave. A discussion of the subject of stimulated Cerenkov radiation can be found in Walsh [1]. Cerenkov masers are attractive sources of radiation at centimeter and millimeter wavelengths [2–4] and have demonstrated high power capabilities [5,6]. Cerenkov masers also have applications in short pulse microwave generation by the SASE mechanism as observed by Wiggins *et al.* [7]. An excellent treatment of the general subject of beam-wave interaction can be found in the text by Schächter [8].

This paper analyzes both the steady state and transient response of the Cerenkov maser for TM_{0n} modes with inhomogeneous electron beams. The linear theory of the Cerenkov maser is discussed in Sec. II, for which there exists a substantial body of literature. Shoucri [9] calculates the dispersive properties and instability growth rates of an unmagnetized electron beam in a dielectric loaded waveguide. Mishra and Tripathi [10] and Kim *et al.* [11] examine the case for an electron beam with finite $\boldsymbol{v}_\perp$ and determine the dispersion relation for both the Cerenkov and cyclotron instabilities. Chang *et al.* [12] consider a finite width sheet beam over a dielectric layer in a rectangular waveguide. They also discuss the dispersion relation for hybrid modes in this geometry as well as mode competition and input and output mode converters to be used in an amplifier system. In addition, Joe *et al.* [13] consider a dispersion analysis for finite width sheet beams propagating over a grating in a rectangular waveguide. Their analysis includes hybrid modes and they examine convective instabilities of the forward waves and absolute instabilities

---

[*] poole1@llnl.gov
[†] blackfield1@llnl.gov
[‡] Frank.Camacho@kirtland.af.mil

of the backward waves. We extend the linear theory to include electron beams that have a parabolic radial inhomogeneity in the equilibrium particle density in a dielectric loaded waveguide. Godfrey [14] addresses the linear theory of unneutralized electron beams in a waveguide for arbitrary radial inhomogeneities in beam energy or beam density by numerically solving the differential equations for the normal modes of the system, but that system did not include dielectric loading and hence does not allow for unstable growth of Cerenkov radiation. We examine the case when the waveguide mode and space-charge waves on the electron beam are coupled and, for the case of a parabolic density profile, determine exact solutions for the dispersion relation and modal structure in terms of confluent hypergeometric functions.

Section III presents a macroparticle model of the Cerenkov amplifier configuration. A macroparticle model is used to determine the saturation of the Cerenkov instability. Lemons and Thode [15] consider both the linear and nonlinear regime of operation of the Cerenkov maser; however, their nonlinear analysis only provides an estimate of the saturation amplitude based on phase trapping of beam electrons. Freund [16] and Freund and Ganguly [17] develop a three-dimensional macroparticle model of the Cerenkov amplifier for weak beams based on models similar to those used for the analysis of gyrotrons and free electron lasers. It has the advantage of reduced computational requirements due to the extraction of the fast behavior of the wave-particle dynamics. This methodology is used to bridge the gap between simple linear models and PIC codes which have much more extensive computational requirements. In their analysis, which assumes weak beams and small growth rates, the waveguide modes are unperturbed by the presence of the electron beam. Near wave-particle synchronism, a set of coupled nonlinear ordinary differential equations are derived for the wave amplitude and phase in terms of the microscopic particle current. These differential equations are closed by the relativistic Lorentz force equation. This technique explicitly extracts the fast spatial behavior of the wave-particle dynamics. In the intense beam regime, PIC codes are used to study the nonlinear properties of Cerenkov amplifiers. Pointon and DeGroot [18] and Weatherall and Main [19] study the Cerenkov amplifier using PIC codes with periodic axial boundary conditions.

Numerical results from the linear theory of Sec. II and the steady-state amplifier model of Sec. III are presented in Sec. IV for a typical amplifier configuration. The dispersion relation is determined for a variety of beam currents and scale lengths of the parabolic density profile. The same system is then examined using the steady-state amplifier model. In the linear regime, the dispersive properties of the system are extracted and compared with that of the linear theory. In addition, phase trapping of the beam electrons and subsequent saturation of the instability is observed. The amplifier efficiency is determined and compared with simple estimates based on energy conservation arguments.

In Sec. V results from PIC simulations of the Cerenkov maser are presented for the single pass transient regime for times less than the transit time of the electron beam through the system. In these simulations microwave generation due to the SASE mechanism results from the injection of a fast rise time electron beam into the Cerenkov maser which seeds the instability. From the results of these simulations, comparisons are made to the linear and macroparticle model results of Sec. IV in the appropriate regimes. Effects such as particle phase trapping and subsequent saturation of the instability are analyzed to estimate the efficiency of the microwave source. Growth rates compare favorably with the results from the linear theory and saturation compares favorably with estimates produced by the macroparticle model of Freund [16] and Freund and Ganguly [17]. Higher power can be achieved in amplifiers by tapering the phase velocity in the amplifier so that the bunches can remain synchronous with the wave for a longer time [20]. Naqvi [20] also achieved higher efficiencies by utilizing bunch compression in a two stage slow wave structure. However, high power in the transient regime can also be achieved because of distributed effects between the electromagnetic field and the bunch, requiring the behavior of the instability in the nonlinear transient regime to be investigated more carefully. SASE driven superradiance has been observed in Cerenkov masers by Ginzburg *et al.* [21] and Jaroszynski *et al.* [22]. In this regime, it is important to include the effect of the slippage of the radiation pulse along the electron beam since the group velocity of the radiation pulse may be significantly slower than the beam velocity. As the pulse continues to evolve in this nonlinear regime, the amplitude may exceed the saturation amplitude as calculated from the steady-state amplifier model and be accompanied by a decreasing pulse width, and a further decrease in group velocity. Simulations show that a series of pulses, typically ~2–6 rf cycles in length, are generated. From the PIC simulations, the evolution of the SASE generated superradiant pulses are examined.

II. LINEAR THEORY

In this section, we examine the linear steady-state response of the Cerenkov maser. We derive a complex dispersion relation for TM_{0n} modes that describe the interaction of a relativistic electron beam with a radial charge density inhomogeneity as it passes through a dielectric loaded circular waveguide. Figure 1 shows the configuration for the Cerenkov maser, consisting of a perfectly conducting cylindrical waveguide of radius R_0 having a dielectric annulus with inner radius R_d located immediately inside the waveguide. An electron beam fills the vacuum region within the dielectric annulus with a parabolic radial density inhomogeneity,

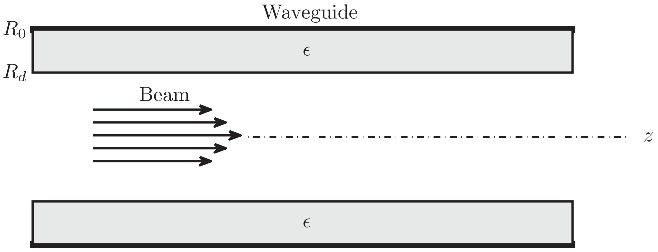

FIG. 1. (Color) Configuration of the Cerenkov maser.

$$n_b(r) = n_0\left(1 + \delta\frac{r^2}{R_d^2}\right) \qquad 0 \le r < R_d, \tag{1}$$

with the restriction that $\delta \ge -1$. The beam has axial velocity v_0, is assumed to be cold, and confined by a large magnetic field so that the beam motion is longitudinal and cyclotron instabilities are unimportant. Assuming a harmonic solution of the form $e^{i(k_z z - \omega t)}$, the defining differential equations for the axial electric field in the beam and dielectric regions are given by

$$\left\{\frac{1}{r}\frac{d}{dr}\left(r\frac{d}{dr}\right) + \kappa^2\left[1 - \frac{\omega_b^2(r)}{\Omega^2}\right]\right\}E_z(r) = 0 \qquad 0 \le r \le R_d, \tag{2}$$

and

$$\left[\frac{1}{r}\frac{d}{dr}\left(r\frac{d}{dr}\right) + \kappa_\epsilon^2\right]E_z(r) = 0 \qquad R_d \le r \le R_0, \tag{3}$$

where the transverse wave numbers are defined for the beam and dielectric regions as

$$\kappa^2 = \frac{\omega^2}{c^2} - k_z^2, \tag{4}$$

$$\kappa_\epsilon^2 = \frac{\epsilon\omega^2}{c^2} - k_z^2, \tag{5}$$

respectively. The beam resonance term is given by

$$\Omega^2 = \gamma^3(\omega - k_z v_0)^2, \tag{6}$$

and the inhomogeneous beam plasma frequency is

$$\omega_b^2(r) = \omega_{b0}^2\left(1 + \delta\frac{r^2}{R_d^2}\right), \tag{7}$$

where $\omega_{b0}^2 = e^2 n_0/m\epsilon_0$, $\gamma = 1/\sqrt{1-\beta^2}$, and $\beta = v_0/c$. For the parabolic density profile defined in Eq. (1), it is possible to find closed form solutions for Eq. (2) which can be cast into a standard form by using the changes of variables,

$$x = i\alpha r^2, \qquad \alpha = i\frac{\sqrt{\delta}\kappa\omega_{b0}}{\Omega R_d}, \qquad Q = \kappa^2\left(1 - \frac{\omega_{b0}^2}{\Omega^2}\right). \tag{8}$$

The equation defining the axial electric field in the beam region can be rewritten as a Kummer differential equation,

$$x\frac{d^2\psi}{dx^2} + (1-x)\frac{d\psi}{dx} + \frac{1}{4}\left(\frac{Q}{i\alpha} - 2\right)\psi = 0, \tag{9}$$

where

$$E_z = E_1\psi e^{-i\alpha r^2/2}, \tag{10}$$

and ψ is the solution to the Kummer differential equation, given by

$$\psi = M\left[\frac{1}{4}\left(2 - \frac{Q}{i\alpha}\right), 1, x\right], \tag{11}$$

where $M(a, b, x)$ is a Kummer function, sometimes denoted as the confluent hypergeometric function ${}_1F_1(a, b, x)$ [23]. The second linearly independent solution to Eq. (9) is logarithmically singular at $r = 0$ and is therefore not included as part of the solution in the beam region for $0 \le r \le R_d$. The solution for the axial electric field in the dielectric annulus region defined by Eq. (3) is given by

$$E_{z\epsilon} = E_2 J_0(\kappa_\epsilon r) + E_3 Y_0(\kappa_\epsilon r). \tag{12}$$

The dispersion relation is obtained by applying boundary conditions to the system, which allows the three undetermined constants E_1, E_2, and E_3 to be related. The boundary conditions for the tangential electric fields are $E_{z\epsilon}(R_0) = 0$ and $E_z(R_d) = E_{z\epsilon}(R_d)$. In addition, the boundary condition for the normal component of electric displacement at the beam-dielectric interface is $E_r(R_d) = \epsilon E_{r\epsilon}(R_d)$, which requires evaluating the radial derivative of the axial electric fields at R_d. The dispersion relation can be written as

$$\frac{i\alpha\kappa_\epsilon R_d}{\epsilon\kappa^2}\left\{1 - \left(1 - \frac{Q}{2i\alpha}\right)\frac{M[\frac{1}{2}(3 - \frac{Q}{2i\alpha}), 2, i\alpha R_d^2]}{M[\frac{1}{4}(2 - \frac{Q}{i\alpha}), 1, i\alpha R_d^2]}\right\} + W = 0, \tag{13}$$

where

$$W = \frac{J_0(\kappa_\epsilon R_0)Y_1(\kappa_\epsilon R_d) - J_1(\kappa_\epsilon R_d)Y_0(\kappa_\epsilon R_0)}{J_0(\kappa_\epsilon R_d)Y_0(\kappa_\epsilon R_0) - J_0(\kappa_\epsilon R_0)Y_0(\kappa_\epsilon R_d)}. \tag{14}$$

It should be noted that the arguments of the Kummer functions in the numerator and denominator of Eq. (13) are different, resulting from evaluating the radial derivative of the Kummer function which is required to evaluate the normal electric displacement at the beam-dielectric interface. It is instructive to look at the limiting case of Eqs. (10), (11), and (13) as $\delta \to 0$. In this case, $\alpha \to 0$, and we have [24]

$$\lim_{\alpha\to 0} M\left[\frac{1}{2}\left(3 - \frac{Q}{2i\alpha}\right), 1, i\alpha r^2\right] = \frac{2}{Q^{1/2}r}J_1(Q^{1/2}r), \tag{15}$$

and

$$\lim_{\alpha\to 0} M\left[\frac{1}{4}\left(2 - \frac{Q}{i\alpha}\right), 1, i\alpha r^2\right] = J_0(Q^{1/2}r). \tag{16}$$

From Eqs. (10) and (11), $E_z = E_1 J_0(Q^{1/2}r)$, which shows that the modal structure of the axial electric field reduces to a Bessel function dependence; the solution for a homogeneous beam. The dispersion relation defined in Eqs. (13) and (14) reduces to the familiar dispersion relation

$$\frac{\kappa_\epsilon}{\epsilon\kappa}\frac{J_1(Q^{1/2}R_d)}{J_0(Q^{1/2}R_d)}\left(1-\frac{\omega_{b0}^2}{\Omega^2}\right)^{1/2}+W=0, \tag{17}$$

for a homogeneous beam.

III. MACROPARTICLE MODEL

A macroparticle model of the Cerenkov instability is required to provide information about the saturation of the instability and the transition from the linear to the saturated regime. Freund and Ganguly [17] have done an extensive 3D analysis of the Cerenkov maser, and in this section we use their formalism to analyze the behavior of our system for TM_{0n} modes. We present the essential features of their analysis in this section but restrict our analysis to 1D motion of the electrons. This analysis assumes the beam is weak ($\omega_b \ll \omega$) so that space-charge effects can be neglected and that the linear spatial growth rate is much less than the axial wave number at synchronism. In this section, the system will be treated as an amplifier by applying a time harmonic signal at $z = 0$. The electromagnetic field in the waveguide is expressed in terms of the normal modes of the system without the presence of the electron beam. The slowly varying amplitude and phase of the electromagnetic field are determined from the dynamics of the electron beam. The axial electric field component can be written as

$$E_z=\sum_{n=1}^{\infty}E_n(z)J_0(\kappa_n r)\cos\Psi_n(z), \tag{18}$$

for $0 \le r \le R_d$, and

$$E_z=\sum_{n=1}^{\infty}E_n(z)[a_nJ_0(\kappa_{\epsilon n}r)+b_nY_0(\kappa_{\epsilon n}r)]\cos\Psi_n(z), \tag{19}$$

for $R_d \le r \le R_0$, where

$$\Psi_n(z)=\int_0^z k_{zn}(z')dz'-\omega t, \tag{20}$$

and the local field amplitudes and the local wave numbers are assumed to be slowly varying functions of z,

$$\left|\frac{1}{E_n}\frac{\partial E_n}{\partial z}\right| \ll k_{zn} \quad \text{and} \quad \left|\frac{1}{k_{zn}}\frac{\partial k_{zn}}{\partial z}\right| \ll k_{zn}. \tag{21}$$

The magnetic field can be determined from the axial electric field as

$$B_\phi=\sum_{n=1}^{\infty}\frac{\omega}{\kappa_n c^2}E_n(z)J_1(\kappa_n r)\sin\Psi_n(z), \tag{22}$$

for $0 \le r \le R_d$, and

$$B_\phi=\sum_{n=1}^{\infty}\frac{\omega\epsilon}{\kappa_{\epsilon n}c^2}E_n(z)[a_nJ_0(\kappa_{\epsilon n}r)+b_nY_0(\kappa_{\epsilon n}r)]\times\sin\Psi_n(z), \tag{23}$$

for $R_d \le r \le R_0$. The constants a_n and b_n are determined from boundary conditions at the waveguide wall and at the vacuum-dielectric interface and are given by

$$a_n=\left(\frac{\pi}{2}\right)\kappa_{\epsilon n}R_d\left[\left(\frac{\kappa_{\epsilon n}}{\epsilon\kappa_n}\right)J_1(\kappa_nR_d)Y_0(\kappa_{\epsilon n}R_d)-J_0(\kappa_nR_d)Y_1(\kappa_{\epsilon n}R_d)\right], \tag{24}$$

and

$$b_n=-\left(\frac{\pi}{2}\right)\kappa_{\epsilon n}R_d\left[\left(\frac{\kappa_{\epsilon n}}{\epsilon\kappa_n}\right)J_1(\kappa_nR_d)J_0(\kappa_{\epsilon n}R_d)-J_0(\kappa_nR_d)J_1(\kappa_{\epsilon n}R_d)\right]. \tag{25}$$

Equation (26) defines the wave equation for the magnetic field in the vacuum region with the macroscopic electron beam current as a source term:

$$\left(\nabla^2-\frac{1}{c^2}\frac{\partial^2}{\partial t^2}\right)\boldsymbol{B}=-\mu_0\nabla\times\boldsymbol{J}. \tag{26}$$

Inserting the magnetic field from Eqs. (22) and (23) into the wave equation defined by (26), neglecting second-order derivatives in amplitude and phase we obtain

$$\sum_{n=1}^{\infty}\frac{\omega}{\kappa_n c^2}J_1(\kappa_n r)\left[\left(\frac{\omega^2}{c^2}-\kappa_n^2-k_{zn}^2\right)E_n\sin\Psi_n+2k_{zn}\frac{\partial E_n}{\partial z}\cos\Psi_n\right]=\mu_0\frac{\partial J_z}{\partial r}. \tag{27}$$

Note that there is only an axial component of electron current since we are considering only 1D electron motion. Similarly, we find for the dielectric region

$$\sum_{n=1}^{\infty}\frac{\omega\epsilon}{\kappa_{\epsilon n}c^2}[a_nJ_1(\kappa_{\epsilon n}r)+b_nY_1(\kappa_{\epsilon n}r)]\times\left[\left(\frac{\omega^2}{c^2}-\kappa_n^2-k_{zn}^2\right)E_n\sin\Psi_n+2k_{zn}\frac{\partial E_n}{\partial z}\cos\Psi_n\right]=0, \tag{28}$$

with $(\omega/c)^2-\kappa_n^2=\epsilon(\omega/c)^2-\kappa_{\epsilon n}^2$. The radial dependence of the magnetic field for TM_{0n} modes satisfies the orthogonality condition [17,25]

$$\sum_j\iint_{S_j}\frac{1}{\epsilon_j}B_{mj}B_{nj}dS_j=A_n\delta_{mn}, \tag{29}$$

where S_j denotes the jth region of the waveguide cross section. Equation (29) becomes

$$-\frac{1}{2}A_nR_d^2\delta_{mn} = \int_0^{R_d} rJ_1(\kappa_m r)J_1(\kappa_n r)dr + \epsilon\frac{\kappa_m\kappa_n}{\kappa_{\epsilon m}\kappa_{\epsilon n}}\int_{R_d}^{R_0} r[a_mJ_1(\kappa_{\epsilon m}r) + b_mY_1(\kappa_{\epsilon m}r)] \times [a_nJ_1(\kappa_{\epsilon n}r) + b_nY_1(\kappa_{\epsilon n}r)]dr, \tag{30}$$

where the constant A_n is

$$A_n = \left(\frac{\epsilon - 1}{\epsilon}\right)\left(-J_1^2(\kappa_nR_d) - \frac{\epsilon k_{zn0}^2}{\kappa_{\epsilon n}^2}J_0^2(\kappa_nR_d) + \frac{2}{\kappa_nR_d}\frac{\epsilon\omega^2}{c^2\kappa_{\epsilon n}^2}J_0(\kappa_nR_d)J_1(\kappa_nR_d)\right) - \epsilon\frac{R_0^2}{R_d^2}\frac{\kappa_n^2}{\kappa_{\epsilon n}^2}[a_nJ_1(\kappa_{\epsilon n}R_0) + b_nY_1(\kappa_{\epsilon n}R_0)]^2. \tag{31}$$

Equations (27) and (28) can be cast into the following form using the orthogonality relation in Eq. (30) and integrating by parts on the right-hand side of Eq. (27):

$$\frac{\omega}{c^2}\left[\left(\frac{\omega^2}{c^2} - \kappa_n^2 - k_{zn}^2\right)E_n\sin\Psi_n + 2k_{zn}\frac{\partial E_n}{\partial z}\cos\Psi_n\right] = \frac{2\mu_0c^2\kappa_n^2}{\omega A_nR_d^2}\int_0^{R_d} rJ_zJ_0(\kappa_nr)dr. \tag{32}$$

By multiplying Eq. (32) by $\cos\Psi_m$ or $\sin\Psi_m$ and averaging over a wave period, we obtain the following equations describing the evolution of the amplitude and phase of the electromagnetic wave in terms of the beam current:

$$2k_{zn}\frac{dE_n}{dz} = \frac{2\mu_0c^2\kappa_n^2}{\pi A_nR_d^2}\int_0^{(2\pi)/\omega}dt\int_0^{R_d} rJ_zJ_0(\kappa_nr)\cos\Psi_ndr, \tag{33}$$

$$\left(\frac{\omega^2}{c^2} - \kappa_n^2 - k_{zn}^2\right)E_n = \frac{2\mu_0c^2\kappa_n^2}{\pi A_nR_d^2}\int_0^{(2\pi)/\omega}dt \times \int_0^{R_d} rJ_zJ_0(\kappa_nr)\sin\Psi_ndr, \tag{34}$$

where the variation in axial wave number is represented in terms of a relative phase $\psi_n(z)$,

$$k_{zn}(z) = k_{zn0} + \frac{d\psi_n}{dz}, \tag{35}$$

and k_{zn0} is the initial wave number determined from the cold dispersion relation. The macroscopic beam current is found by summing over the individual trajectories of an ensemble of individual electrons,

$$J_z(z, \tau_{pq}) = -en_b(r_q)\frac{2\pi v_0}{\omega N_\tau}\sum_{p=1}^{N_\tau}\delta[\tau - \tau_{pq}(z)], \tag{36}$$

where $\tau = \omega t$, and N_τ is the number of macroparticles distributed over 2π in phase. The relativistic dynamical equations can now be written for the (pq)th macroparticle and the nth mode as

$$\frac{d\tau_{pq}}{dz} = \frac{\omega}{c\beta_{pq}} = \frac{k_0}{\beta_{pq}}, \tag{37}$$

and

$$\frac{d\beta_{pq}}{dz} = -\frac{e}{mc^2}\left[\frac{(1-\beta_{pq})^{3/2}}{\beta_{pq}}\right]E_n(z)J_0(\kappa_nr_q) \times \cos\left(k_{zn0}z + \frac{d\psi_n}{dz}z - \tau_{pq}\right). \tag{38}$$

Equations (33)–(38) constitute $2N_rN_\tau + 2$ differential equations (N_rN_τ equations for particle phase, N_rN_τ equations for particle velocity, and two equations for the wave amplitude and phase) which can be solved numerically for each mode. The particles enter the amplifier uniformly distributed in phase.

IV. NUMERICAL RESULTS

For the numerical calculations, we assume the following parameters for the waveguide structure: $R_0 = 2$ cm, $R_d = 1.5$ cm, and $\epsilon = 4$. The electron beam has an energy of 340 keV and an injected beam current I_b ranges from 5 to 500 A. Various scale lengths for the density inhomogeneity are chosen, ranging from $\delta = -1$, to uniform ($\delta = 0$), to $\delta = 25$ in Eq. (1). These parameters were chosen to provide an operating frequency near 8 GHz for the TM_{01} mode and 26 GHz for the TM_{02} mode with spatial growth rates that are sufficiently large to saturate the instability within a 2 m length of the dielectric loaded waveguide. This set of parameters is fairly typical of experimental devices operating in the microwave regime.

The dispersion relation for the two lowest order TM_{0n} modes without an electron beam is shown in Fig. 2 along with the beam line for a 340 keV electron beam intersecting the TM_{01} and TM_{02} modes at 8.12 and 26.26 GHz, respectively, while Fig. 3 shows the mode structure of these modes at the 8.12 and 26.26 GHz operating points. Figure 4 shows the real part of the dispersion relation for the fully coupled system calculated from Eqs. (13) and (14) with an electron beam current of 50 A and $\delta = 1$ for the TM_{01} and TM_{02} modes. Figure 5 shows the normalized spatial growth rate, $\Gamma_nR_d = -\mathrm{Im}(k_{zn})R_d$ for the TM_{01} and TM_{02} modes for a 50 A beam with $\delta = 1$. The maximum spatial growth rates occur at 8.12 and 26.26 GHz for the TM_{01} and TM_{02} modes, respectively.

Numerical simulations of the steady-state amplifier configuration defined by Eqs. (33)–(38) were solved for the TM_{01} and TM_{02} modes for our set of parameters using $N_r = 30$ and $N_\tau = 128$ which conserved energy to within 0.1% for both TM_{01} and TM_{02} modes. Figures 6 and 7 show the evolution of the microwave power and average beam energy for the TM_{01} and TM_{02} modes. The evolution of growth rate and wave number is shown in Figs. 8 and 9.

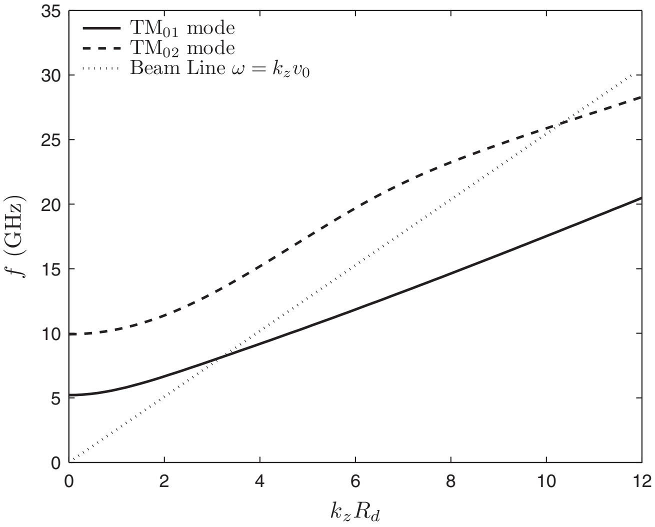

FIG. 2. Cold dispersion relation for the Cerenkov maser for the TM$_{01}$ and TM$_{02}$ modes with $R_0 = 2$ cm, $R_d = 1.5$ cm, and $\epsilon = 4$ showing the beam line with $\beta = 0.8$ (340 keV).

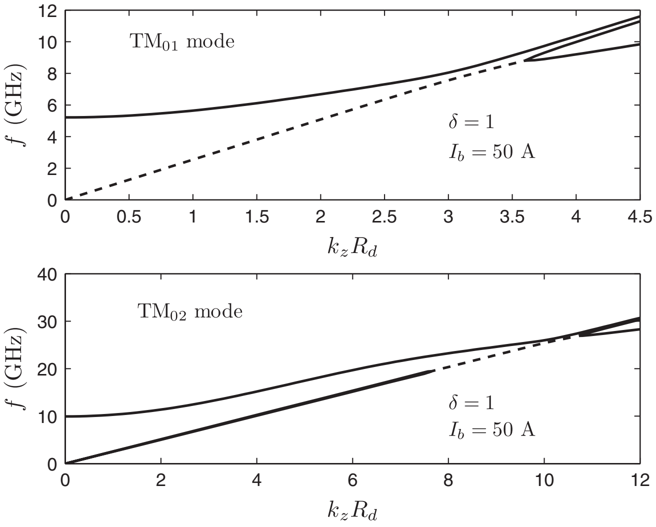

FIG. 4. Real part of TM$_{01}$ and TM$_{02}$ dispersion relation for 50 A beam with $\delta = 1$. The unstable regions of the dispersion relation are shown in the dashed lines.

Defining an instantaneous growth rate as

$$G_n(z) = \frac{1}{E_{zn}} \frac{dE_{zn}}{dz} \tag{39}$$

allows an average normalized growth rate and normalized wave number to be extracted in the region of exponential growth as shown in Figs. 8 and 9. There are three distinct regions of interaction: spatial lethargy, exponential growth, and saturation. During spatial lethargy ($z < 0.2$ meter), the spatially growing wave is not yet dominant and the electrons have not established the correct synchronous condition in a decelerating phase of the wave for maximum exchange of energy. Schächter [26] estimates the lethargy length, d_{ln}, as

$$d_{ln} = \frac{1.412\sqrt{3}}{2\Gamma_n}. \tag{40}$$

For our set of parameters, the lethargy length is estimated to range from (0.1 meter $< z < 0.2$ meter) depending on the mode and the maximum spatial growth rate. This is consistent with Figs. 6 and 7. When the correct synchronism is established, the exponential growth region of operation is entered (0.2 meter $< z < 0.8$ meter) until the wave saturates ($z > 0.8$ meter) where the electrons have lost sufficient energy to slip into an accelerating phase of the wave and execute synchrotron oscillations. The input

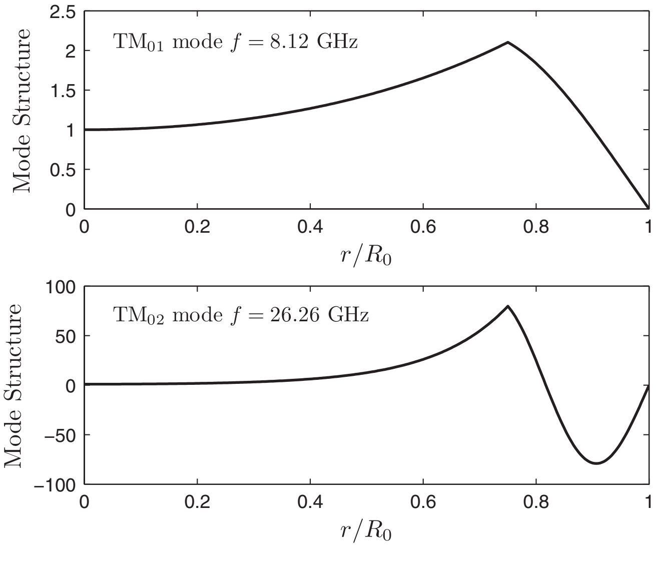

FIG. 3. Mode structure for TM$_{01}$ and TM$_{02}$ modes at 8.12 and 26.26 GHz. Note that the mode amplitude for the TM$_{02}$ mode is unity at $r = 0$.

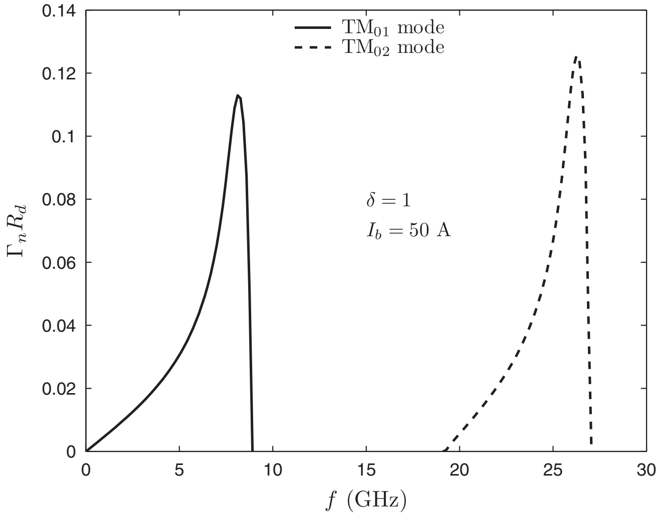

FIG. 5. Normalized spatial growth rates for TM$_{01}$ and TM$_{02}$ modes for a 50 A beam with $\delta = 1$.

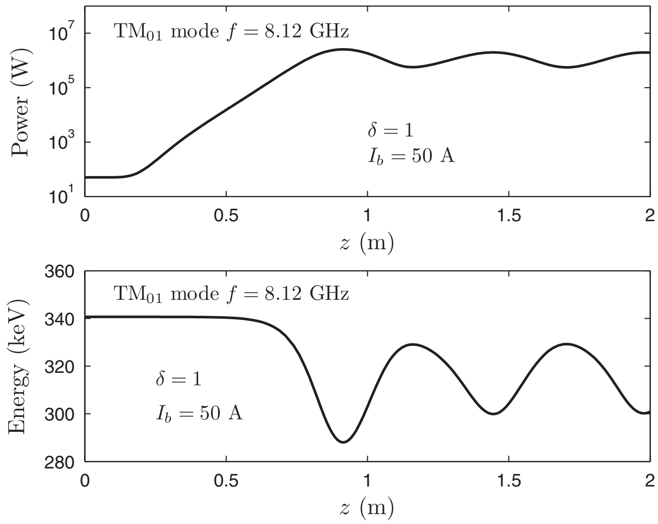

FIG. 6. TM$_{01}$ power at 8.12 GHz and beam energy loss.

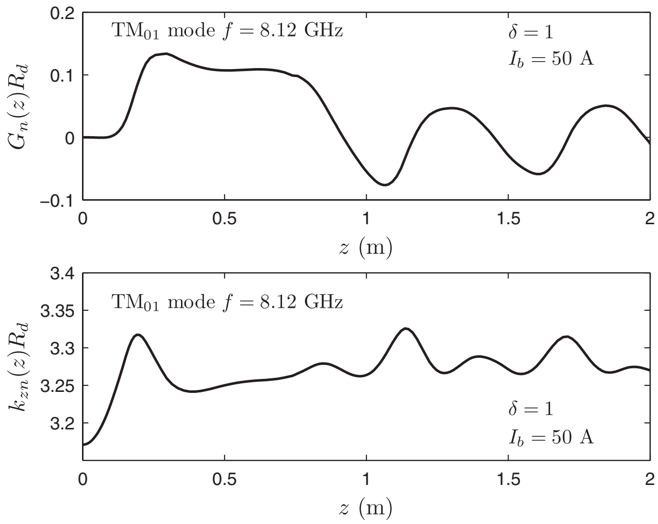

FIG. 8. TM$_{01}$ instantaneous normalized growth rate and wave number at 8.12 GHz.

power to the amplifier for the TM$_{01}$ mode is 51 W with the maximum saturated power of 2.55 MW occurring at $z = 0.8$ m. The corresponding average beam energy at saturation is 288 keV, a 52 keV beam energy loss. Similarly for the TM$_{02}$ mode, the input power is 6.4 W with a maximum saturated power of 600 kW occurring at $z = 0.8$ m. In this case, the average beam energy at saturation is 328 keV, a 12 keV beam energy loss. The maximum saturated conversion efficiencies for the TM$_{01}$ and TM$_{02}$ modes are 15% and 3.5%, respectively. In the region of exponential growth the spatial growth rate and axial wave number are not constant due to the evolving beam-wave dynamics during the interaction. The average normalized growth rate and normalized wave number for the TM$_{01}$ mode is $\langle G_n R_d \rangle = 0.12$ and $\langle k_{zn} R_d \rangle = 3.26$, identical to results from the linear theory. Similarly, for the TM$_{02}$ mode we have $\langle G_n R_d \rangle = 0.13$ and $\langle k_{zn} R_d \rangle = 10.4$, again the same as linear theory predictions. The difference between the initial electron beam velocity and the phase speed of the electromagnetic wave represents, in an average sense, a loss of beam energy, providing a simple model for calculating the average conversion efficiency of the Cerenkov maser. The efficiency, denoted by η, can be estimated as

$$\eta = \frac{\gamma_0 - \gamma_s}{\gamma_0 - 1}, \tag{41}$$

where $\gamma_s = 1/\sqrt{1 - \beta_s^2}$ and $\beta_s = \omega/\langle k_{zn} \rangle$. This estimates the average conversion efficiency at 10% and 3% for the TM$_{01}$ and TM$_{02}$ modes, respectively. It should be noted that the average conversion efficiency is less than the results from the macroparticle model, since the maximum saturated conversion efficiency is determined at the maxi-

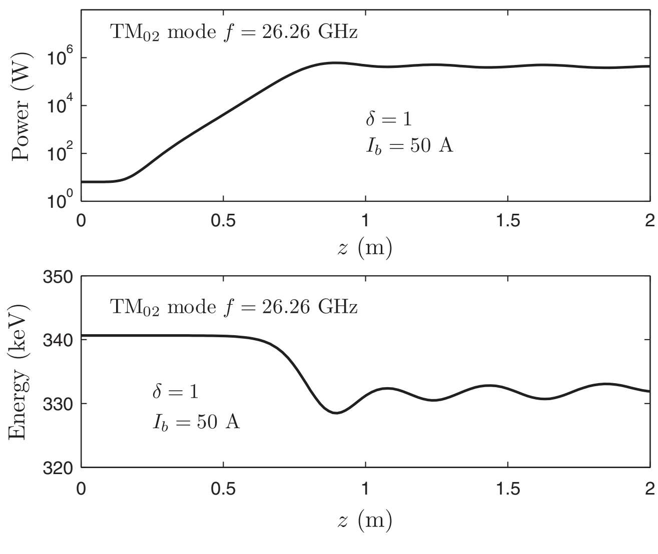

FIG. 7. TM$_{02}$ power at 26.26 GHz and beam energy loss.

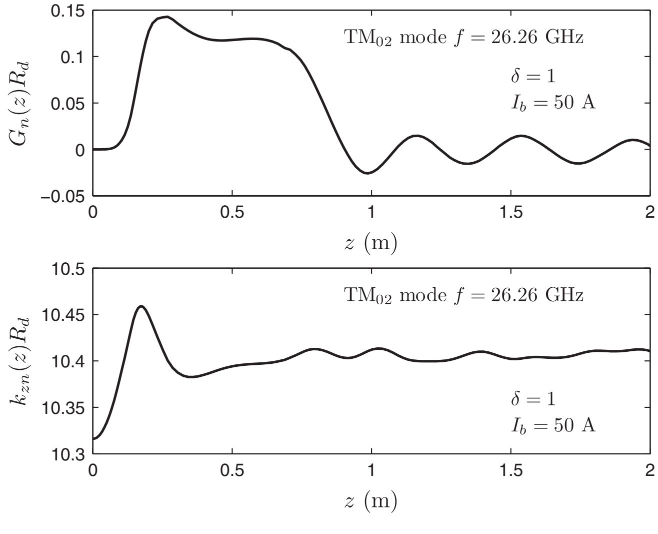

FIG. 9. TM$_{02}$ instantaneous normalized growth rate and wave number at 26.26 GHz.

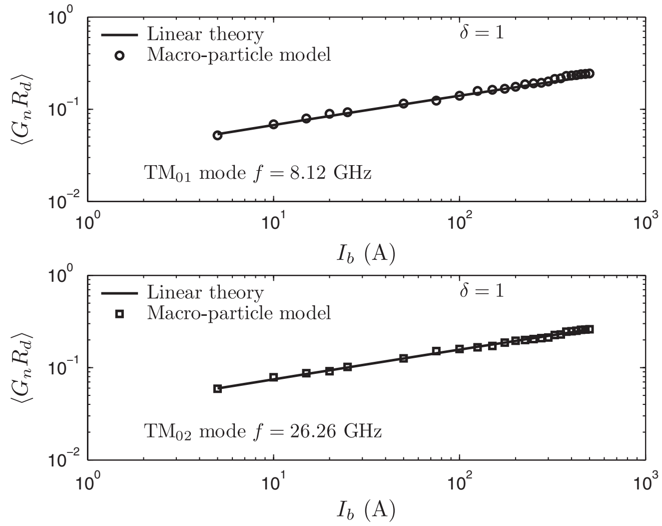

FIG. 10. Normalized growth rates for TM$_{01}$ and TM$_{02}$ modes as a function of beam current for $\delta = 1$. Both spatial growth rates are proportional to $I_b^{1/3}$.

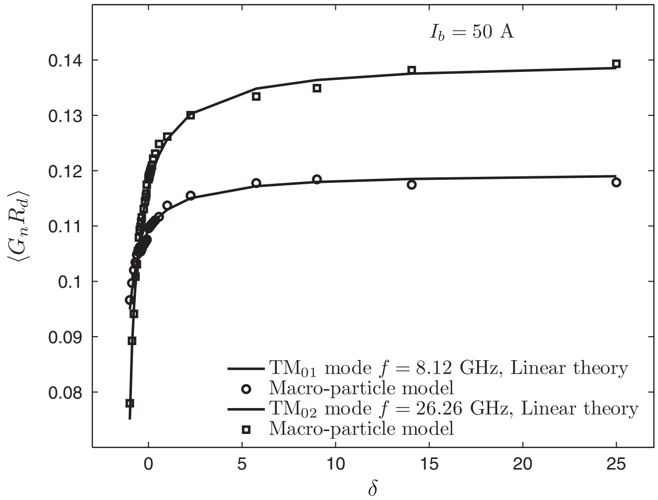

FIG. 12. Normalized growth rates for TM$_{01}$ and TM$_{02}$ modes as a function of inhomogeneity scale factor for a 50 A beam.

mum output power before the wave has had a chance to give back some of its energy to the beam after saturating. The synchrotron oscillations present after saturating are varying about an average beam energy associated with the wave's phase velocity, β_s which is representative of the average conversion efficiency.

It is well known that for a Cerenkov maser operating in the weak beam limit ($\omega_b \ll \omega$) the spatial growth rate of the unstable wave is proportional to $I_b^{1/3}$ [27] for a given beam energy. Figure 10 shows the maximum normalized spatial growth rates for the TM$_{01}$ and TM$_{02}$ modes for a beam with $\delta = 1$ showing the $I_b^{1/3}$ dependence. Similarly, Fig. 11 shows the real part of the normalized axial wave number for the same set of parameters. Figure 12 shows the effect of the scale length of the beam inhomogeneity and that the growth rate is improved as the beam current becomes more localized at the vacuum-dielectric interface. This is to be expected since the transverse wave number in the beam region, κ_n, is imaginary for the Cerenkov instability resulting in a stronger axial electric field near the interface as shown in Fig. 3. It is reasonable to assume that the strength of the interaction is proportional to the axial electric field and the number of electrons available to participate in the interaction at a particular radius. Since $E_z \sim J_0(\kappa_n r)$, the growth rate Γ_n scales as

$$\begin{aligned} F_n &= \frac{2\pi}{k_{zn0}} \int_0^{R_d} r n_b(r) J_0(\kappa_n r) dr \\ &= \frac{2\pi n_0}{k_{zn0}\kappa_n^2} [(1+\delta)\kappa_n R_d J_1(\kappa_n R_d) - 2\delta J_2(\kappa_n R_d)], \end{aligned} \tag{42}$$

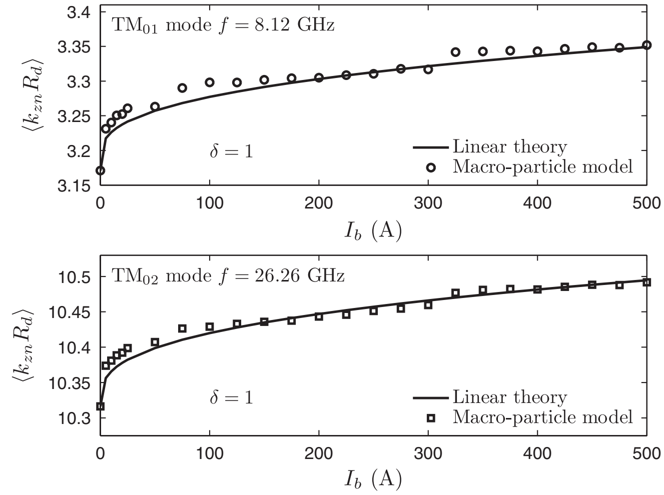

FIG. 11. Normalized wave numbers for TM$_{01}$ and TM$_{02}$ modes as a function of beam current for $\delta = 1$.

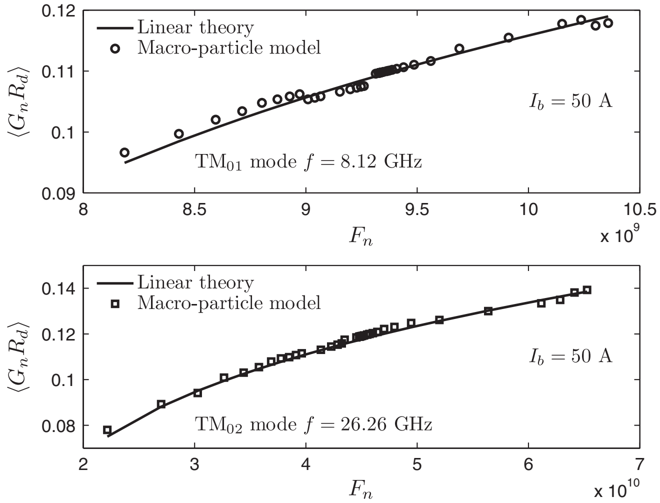

FIG. 13. Normalized growth rates for TM$_{01}$ and TM$_{02}$ modes as a function of coupling parameter, F_n for a 50 A beam.

where $n_b(r)$ is defined in Eq. (1) and k_{zn0} is the solution of the cold dispersion relation. Plots of the maximum spatial growth rates at 8.12 and 26.26 GHz for the TM_{01} and TM_{02} modes are shown in Fig. 13 as a function of the integral defined in Eq. (42). From the previous section describing the macroparticle approach, this coupling integral appears as a driving term for the beam-wave interaction. Figures 10–13 show excellent agreement for the normalized growth rates and wave numbers as predicted from the linear and nonlinear models. The small variations can be attributed to the fact that the beam-wave dynamics do not exhibit pure exponential growth in the steady-state amplifier model.

V. TRANSIENT, SASE PIC SIMULATIONS

LSP [28] is an electromagnetic PIC code, originally developed by Mission Research Corporation. It is designed for plasma or beam simulations in 1D, 2D, or 3D geometries using either an explicit or implicit particle push. We use LSP in 2D axially symmetric geometry with an explicit particle push to model the Cerenkov microwave source. Since PIC codes can be inherently noisy, LSP can employ various spatial and temporal filtering algorithms to reduce noise. We examine the transient behavior of the Cerenkov amplifier when driven by an electron beam with a fast rise time. When the system is driven in this configuration, coherent spontaneous emission (CSE) associated with the spectral content of the fast rising electron beam current pulse provides the seed for the instability allowing for self-bunching of the electron beam. Since the radiation pulse occurs on short time scales less than the single pass transit time of the device, numerical noise has not been an issue for these simulations. SASE and superradiance initiated by CSE have been observed in the Cerenkov maser [7,21,22]. Using PIC simulations, we can extract parameters associated with both the linear and nonlinear regimes of operation. In addition, other nonlinear processes can be examined such as superradiance which is not predicted by the steady-state amplifier model. Also, details of the microwave pulse shape can be determined accurately in the linear regime, from the beam injection point through the asymptotic linear regime prior to nonlinear saturation using conventional transform techniques.

Spontaneous emission can arise from two sources; incoherent spontaneous emission associated with random phase variations of the electrons relative to the wave, and CSE associated with the longitudinal structure of the electron current density. In cases where the longitudinal electron current has spatial variations on the order of the radiation wavelength, the coherent component may dominate over the incoherent component of spontaneous emission by many orders of magnitude [29]. With incoherent spontaneous emission the radiation intensity scales linearly with current. The incoherent component of spontaneous emission can be estimated from the steady-state saturated power by [7,29]

$$P_{\mathrm{incoh}} \sim \frac{P_{\mathrm{sat}}}{N_c}, \tag{43}$$

where N_c is the number of electrons within a cooperation length (coherence length). The cooperation length is $l_c = Sl_g$, where l_g is the gain length, with $l_g = 1/\Gamma$, where Γ is the spatial growth rate, and S is the slippage parameter,

$$S = \left(1 - \frac{v_g}{v_0}\right), \tag{44}$$

where $v_g = \partial\omega/\partial k_z$ is the group velocity of the radiation. In the case of CSE the radiation intensity scales quadratically with current. The coherent component of spontaneous emission is estimated as [7,29]

$$P_{\mathrm{coh}} \sim P_0(\omega) N_c^2 \mid n(\omega) \mid^2, \tag{45}$$

where $P_0(\omega) = P_{\mathrm{incoh}}/N_c$ is the power radiated by a single electron and $n(\omega)$ is the Fourier transform of the longitudinal electron density function. The total spontaneous emission is then

$$\begin{aligned} P_{\mathrm{spon}}(\omega) &= P_{\mathrm{incoh}}(\omega) + P_{\mathrm{coh}}(\omega) \\ &= P_0(\omega)N_c + P_0(\omega)N_c^2|n(\omega)|^2. \end{aligned} \tag{46}$$

For these simulations, the coherent component of spontaneous emission dominates over the incoherent component of spontaneous emission. For the TM_{01} mode, the nonlinear steady-state model predicts that the saturated power is 2.55 MW for a 50 A beam with $\delta = 1$. The cooperation length is 2.5 cm (see calculation later in this section) yielding $N_c \sim 3.25 \times 10^{10}$ electrons within a cooperation length, which results in approximately 78.5 μW of incoherent spontaneous emission.

The geometry described in the earlier sections was simulated with the LSP PIC code in r-z geometry with mesh cell sizes of $\Delta r = \Delta z = 0.5$ mm and a constant time step of $\Delta t = 0.5$ ps. The total number of mesh cells was 8×10^4 with a maximum of $\sim 10^7$ macroparticles. A 340 keV electron beam with a leading edge of the form

$$I_b(t) = \frac{I_{b0}}{2}(1 - \cos\omega_0 t) \qquad t \le \pi/\omega_0 \tag{47}$$

was injected into a 2 m long structure with $\omega_0/2\pi = 8.12$ GHz, where the gain is maximum for the TM_{01} mode. This results in a rise time of $\pi/\omega_0 = 61.6$ ps. After rising to a constant value the beam pulse current remained at a constant value for about 8 ns. The form in Eq. (47) is chosen since dI_b/dt is continuous which reduces high frequency numerical noise in the simulations while providing a significant seed signal at a frequency corresponding to the maximum spatial gain. It is found that the coherent component of spontaneous emission for this current pulse is approximately 64 W, a factor of 8×10^5 larger than the incoherent component of spontaneous emission. A variety of beam currents and inhomogeneity scale lengths are simulated and compared with the results from the linear and macroparticle models for the TM_{01} mode which was the dominant mode excited in this system. To excite higher order TM_{0n} modes would require the seed signal at the requisite frequency to be enhanced by prebunching of the electron beam. Small levels of TM_{02} and higher order modes were observed in the simulations.

We will first extract parameters from the PIC simulations to compare with results from the linear theory for the TM_{01} mode. We will then demonstrate a scaling relation for SASE power production in the linear regime due to CSE associated with the leading edge of the electron beam. Next, the nonlinear processes associated with saturation due to phase trapping of the electrons will be examined. It is also found that microwave power continues to grow beyond the steady-state nonlinear saturation level, accompanied by a shift in frequency and axial wave number. In addition, this superradiant regime is characterized by microwave pulse compression and the emergence of several radiation pulses.

Figure 14 shows a typical pulse shape for the axial electric field at three spatial locations along the z axis of the Cerenkov maser, in this case for a 50 A beam with $\delta = 1$. The source of the emission is CSE associated with the pulse shape for the leading edge of the electron beam. Similarly, Fig. 15 shows the spatial structure of the microwave pulse at three instants of time.

There are several features to be noted with the microwave pulses shown in Figs. 14 and 15. First, the radiation pulse is slipping further behind the head of the beam since the group velocity is significantly lower than the beam velocity. Second, the frequency and wave number shift to larger values as the pulse evolves due to the shift in the resonance term in the dispersion relation as the beam loses energy and the instability is detuned. As the frequency and wave number shift, the group velocity of the pulse decreases, and the pulse slips further behind the beam head. Third, the pulse width decreases as the radiation pulse enters this nonlinear superradiant regime accompanied by significant spectral broadening. In addition, subsequent pulses emerge behind the beam head, whose characteristics are determined primarily by the nonlinear dynamics of the strongly bunched beam in this region.

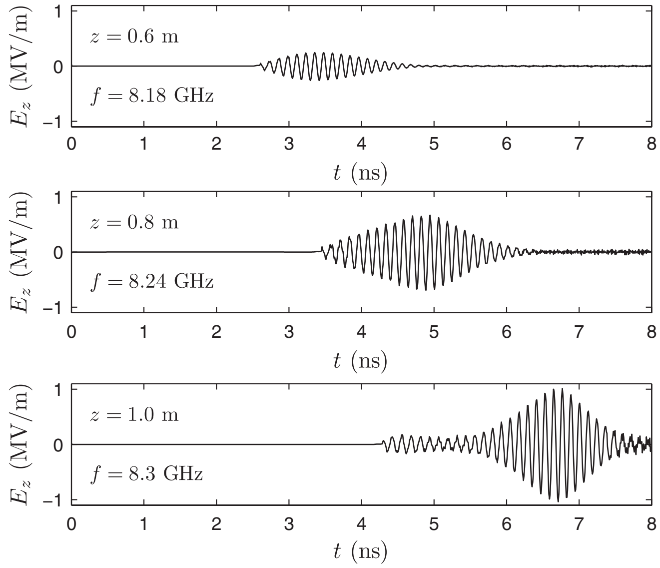

FIG. 14. Temporal pulse evolution for a 50 A beam with $\delta = 1$ showing shift in resonant frequency from 8.18 GHz in the linear regime to 8.3 GHz in the nonlinear regime as the pulse evolves.

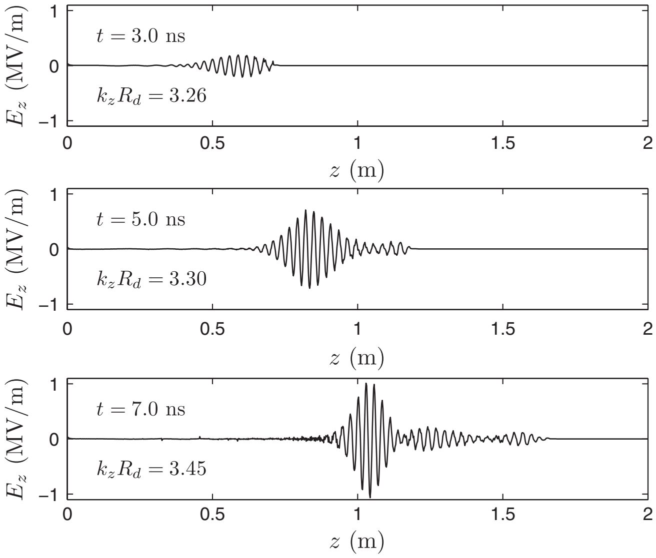

FIG. 15. Spatial pulse evolution for a 50 A beam with $\delta = 1$ showing shift in resonant wave number from $k_zR_d = 3.26$ in the linear regime to $k_zR_d = 3.45$ in the nonlinear regime as the pulse evolves.

The electric field, $E_z(z, t)$, is Fourier transformed in the usual manner,

$$\mathcal{E}_z(k_z, \omega) = \int_{-\infty}^{\infty}\int_{-\infty}^{\infty} E_z(z, t)e^{-i(k_z z-\omega t)}dtdz, \qquad (48)$$

to extract the spectral content and the gain associated with the radiation pulse. The dominant frequency and wave number extracted from the radiation pulse in the linear regime is 8.18 GHz and 217.1 m^{-1}, respectively. From this transform operation the spatial gain Γ_n is extracted as a function of frequency as shown in Fig. 16. As can be seen there is very good agreement between the PIC simulation and the linear theory. Figures 17–19 demonstrate the expected scaling when compared with the linear theory for a variety of beam currents and coupling parameters.

Since, in the linear regime the electric field scales as $E_{z0}e^{\Gamma_n z}$, where E_{z0} is the initial electric field associated with CSE, and $E_{z0} \propto dI_b/dt$, the SASE power in the linear regime should scale as

$$P(I_{b0}) \propto \omega(I_{b0})k_z(I_{b0})I_{b0}^2 e^{2\Gamma_n(I_{b0})z}, \qquad (49)$$

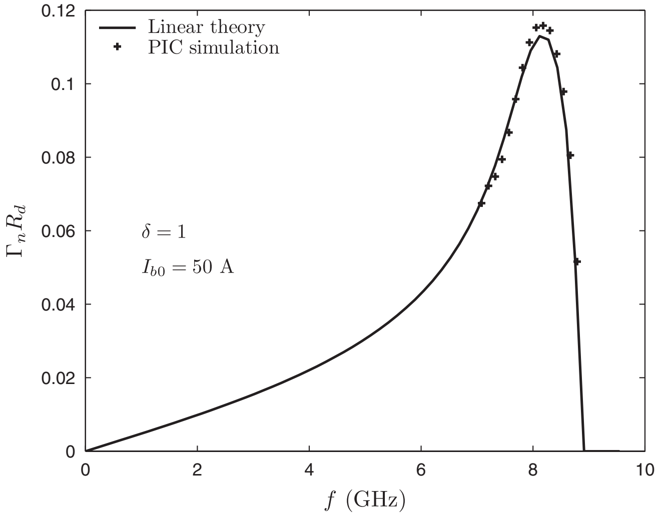

FIG. 16. Normalized spatial growth rates for TM_{01} mode for a 50 A beam with $\delta = 1$.

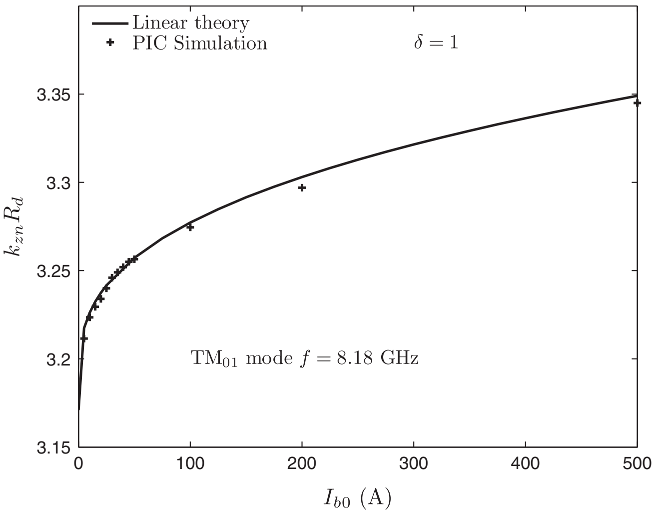

FIG. 18. Normalized wave number for the TM_{01} mode as a function of beam current for $\delta = 1$.

where ω and k_z are only weakly dependent on I_{b0} in the Compton or weak beam limit. This scaling has been discussed in recent work on SASE and superradiance in Cerenkov masers [7,22] and is shown in Fig. 20. Figure 21 shows the evolution of the longitudinal phase space of the beam at three points in time. Strong modulation of the beam longitudinal momentum is observed at $t = 3$ ns, the onset of phase trapping of the beam electrons is being established at $t = 5$ ns, and the particles are strongly trapped at $t = 7$ ns. It can be seen in Fig. 21 that the onset of trapping occurs at a $\gamma\beta \approx 1.2$ corresponding to a beam energy of approximately 287 keV. This energy corresponds to a 53 keV energy loss consistent with the results from the macroparticle model. The particles exhibit strong synchrotron oscillations in the nonlinear regime at the synchrotron frequency

$$\omega_s = \left[-\frac{\omega_0 e E_s \sin\varphi_s}{\beta_s \gamma_s^3 mc} \right]^{1/2}, \tag{50}$$

where ω_0 is the rf frequency, E_s is the peak electric field at saturation, $\beta_s c$ is the synchronous velocity, $\gamma_s = 1/\sqrt{1 - \beta_s^2}$, and $\varphi_s = -\pi/2$ is the synchronous phase at saturation. The wave number associated with synchrotron oscillations is $k_s = \omega_s/\beta_s c$. It was found from the results of the macroparticle model discussed in Sec. IV that the saturation electric field for the TM_{01} mode is ~ 1 MV/m and $\gamma_s\beta_s = 1.25$, resulting in a synchrotron wavelength, $\lambda_s = 2\pi/k_s$, of approximately 0.48 m as seen in Fig. 6.

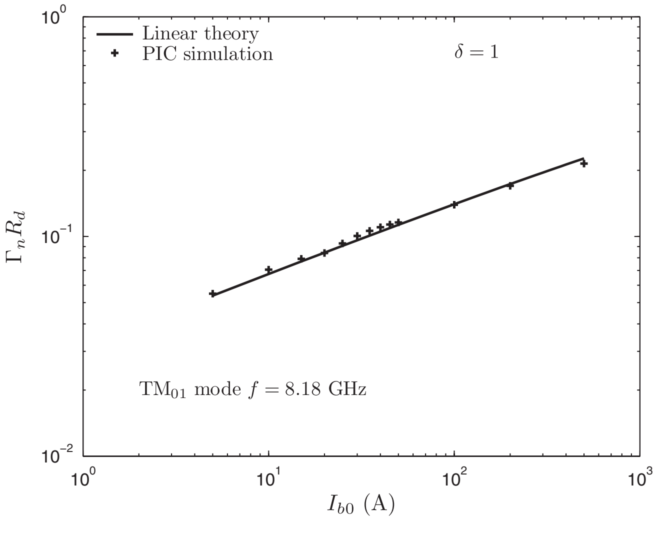

FIG. 17. Normalized growth rates for TM_{01} mode as a function of beam current for $\delta = 1$. Spatial growth rate is proportional to $I_b^{1/3}$.

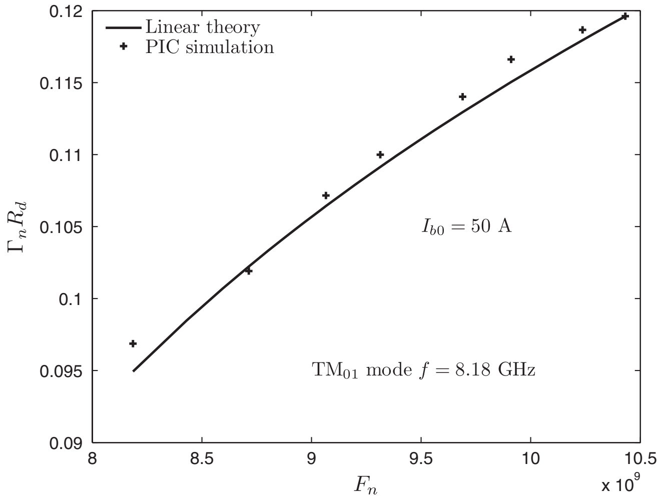

FIG. 19. Normalized growth rates for the TM_{01} mode as a function of coupling parameter, F_n.

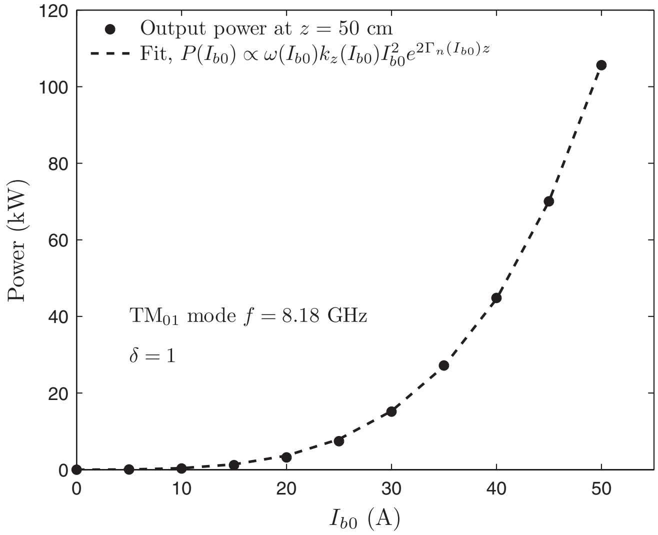

FIG. 20. Scaling of SASE power in the linear regime at $z = 0.5$ meter with a beam current for the TM_{01} mode.

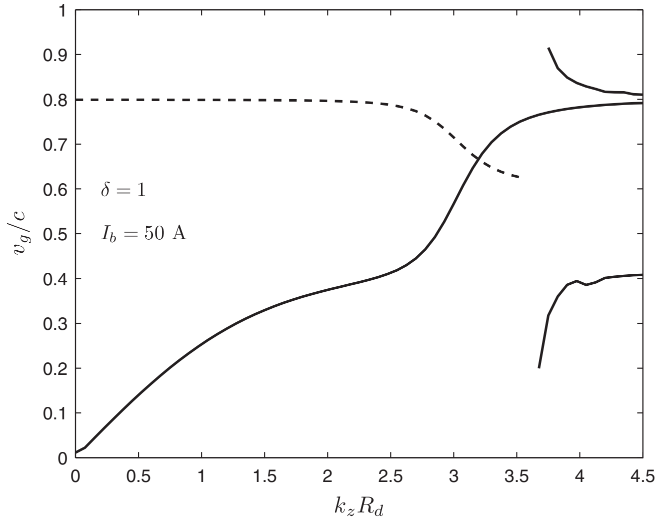

FIG. 22. Group velocity for a 50 A beam with $\delta = 1$ from the dispersion relation in Fig. 4. The unstable branch of the dispersion relation is shown in the dashed line.

The details of saturation in the transient regime associated with SASE and superradiant emission are somewhat more complicated than in the steady-state nonlinear model due to the details of the spectral content of the radiation pulse, the gain of the amplifier, and the slippage of the radiation pulse along the beam. Figure 22 shows the group velocity as calculated from the TM_{01} dispersion relation shown in Fig. 4. The group velocity of the unstable mode near $k_z R_d = 3.26$ is approximately $0.65c$ resulting in a slippage factor of $S \approx 0.19$. The spatial growth rate of the TM_{01} mode at 8.18 GHz is approximately 7.7 m^{-1}, resulting in a cooperation length of 2.5 cm. As the beam advances a distance l_g, the radiation advances a factor of $(1 - S)l_g$ along the beam. As the instability detunes, the wave number shifts to larger values (see Fig. 15) and as can be seen in Fig. 22 the group velocity will decrease. From the PIC simulations, the peak of the radiation pulse is tracked to determine the group velocity as shown in Fig. 23. This is done by evaluating the Hilbert transform of the temporal pulse at each spatial location along the z axis and determining the location of the maximum of the magnitude of the Hilbert transform. As can be seen in Fig. 23, the group velocity, dz_r/dt_r, is decreasing as the radiation pulse increases in amplitude, with an especially

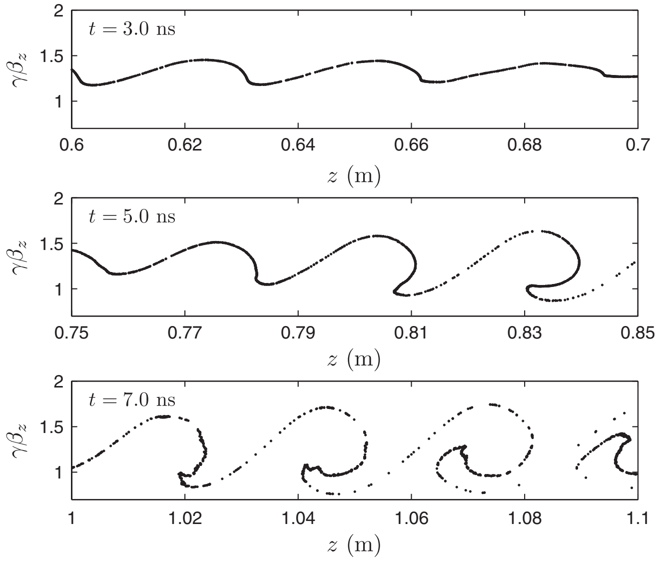

FIG. 21. Longitudinal phase space evolution for a 50 A beam with $\delta = 1$ showing phase trapping of beam electrons and the onset of synchrotron oscillations.

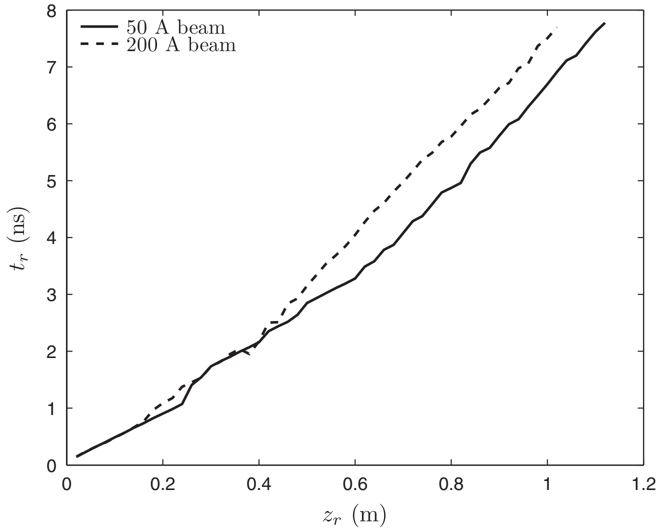

FIG. 23. Trajectory of peak of radiation pulse for a 50 A and a 200 A beam with $\delta = 1$ from PIC simulations. The group velocity is the inverse slope of the characteristic associated with the peak of the radiation pulse.

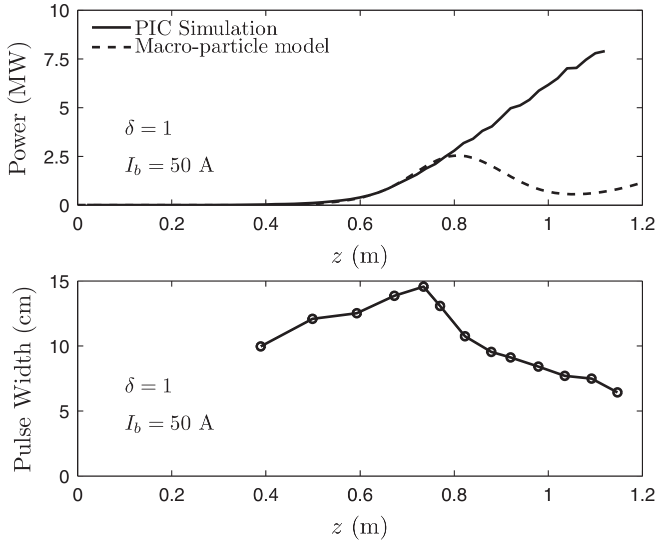

FIG. 24. Microwave power for superradiant pulse and the steady-state result for a 50 A beam with $\delta = 1$. The pulse width decreases as the pulse enters the superradiant regime.

strong effect as the pulse nears saturation. z_r and t_r denote the characteristic defining the peak of the radiation pulse. In the linear regime for $z < 0.6$ meter it is found that $v_g = 0.65c$, consistent with linear theory, but decreases to $v_g \sim 0.45c$ as the pulse enters the nonlinear regime. Figures 24 and 25 show the peak output power and spatial pulse width (FWHM), σ, of the radiation intensity along the amplifier for beam currents of 50 and 200 A, respectively, along with results from the steady-state amplifier model. The input power for the steady-state amplifier model is adjusted to match the approximate initial power produced by CSE associated with the leading edge of the electron beam pulse. As can be seen in Fig. 24 and 25, the pulse grows exponentially in the linear regime with an increasing pulse width due to dispersion. The superradiant pulse then continues to grow past steady-state nonlinear saturation with an accompanying decrease in pulse width. While the superradiant pulse for the 50 A case does not saturate within the length of the simulation, the 200 A case saturates at approximately 0.8 m with a peak power of 36 MW and a pulse width of approximately $\sigma = 2.7 l_c = 4.6$ cm ($\sim$3–4 rf cycles). In contrast, the maximum saturated steady-state power as calculated from the steady-state amplifier model is approximately 12 MW for a 200 A beam. The intensity of the superradiant pulse scales linearly with distance and the pulse width, σ, scales as $\sigma \propto 1/\sqrt{z}$ as seen in Figs. 24 and 25. As the pulse continues to propagate after saturating at $z \sim 0.8$ meter, the pulse width starts to increase as dispersive effects start to dominate. Growth of the superradiant pulse is ultimately limited by reaching a pulse length on the order of several cooperation lengths. Power levels on the order of 100 MW with a pulse width on the order of $\sigma = 2.4 l_c = 3.2$ cm ($\sigma \sim 2$ rf cycles) were observed in the simulations. Figure 26 shows the superradiant (SR) growth rate, $\Gamma_{\rm SR}$, as a function of beam current.

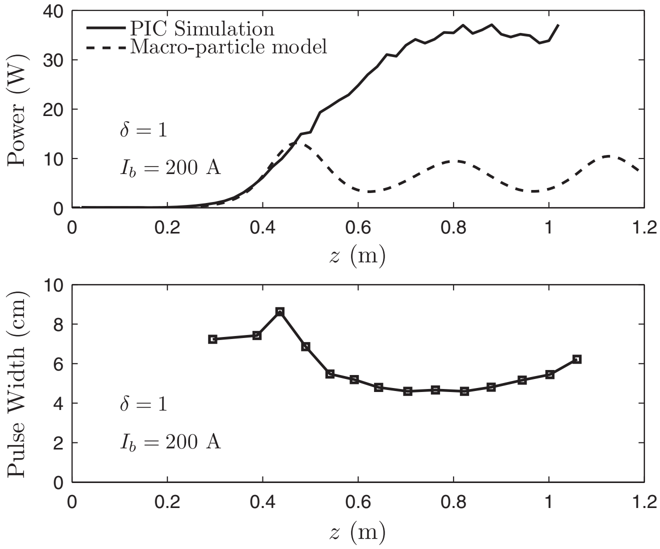

FIG. 25. Microwave power for superradiant pulse and the steady-state result for a 200 A beam with $\delta = 1$. The pulse ultimately saturates as the pulse width approaches the cooperation length.

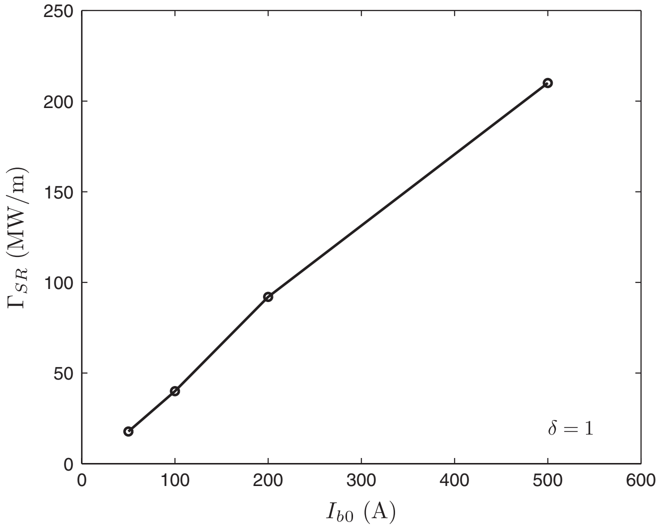

FIG. 26. Growth rate of the radiation pulse in the superradiant regime.

VI. CONCLUSION

We have presented a comprehensive examination of the Cerenkov maser using three models of increasing complexity. First, the linear model was extended to include electron beams with a radial parabolic density profile. The dispersion relation for this system was calculated as well as the modal structure of the electromagnetic field, with the solutions approaching the results of the limiting case of a uniform electron beam. The gain followed the well-known scaling law with beam current ($\Gamma \propto I_b^{1/3}$) in the weak beam limit. It was found that the gain could be enhanced by changing the scale length of the parabolic beam profile so that more electrons participate in the interaction near the beam-dielectric interface. Second, a steady-state amplifier model based on the work of Freund and Ganguly [17] was used to determine the saturation amplitude of the amplifier. The results of this model in the exponential gain regime agreed with predictions from the linear theory for a large range of beam currents and radial scale lengths of the profiled electron beam. Third, PIC simulations were used to examine the SASE and superradiant regimes of the Cerenkov maser when driven with a fast rise time electron beam. In the linear regime, the PIC results agreed with both the linear model and the steady-state amplifier model. The scaling of SASE output power with beam current agreed with simple scaling arguments in the exponential gain regime. However, the dynamics are significantly altered due to the effect of slippage of the radiation pulse behind the beam head. It was shown that, as the pulse slips further behind the head of the beam, amplification can continue beyond steady-state nonlinear saturation levels as the Cerenkov instability is detuned. As the superradiant pulse evolves, the pulse width decreases until it approaches the cooperation length and the pulse saturates.

ACKNOWLEDGMENTS

The authors would like to thank Dr. George J. Caporaso for helpful discussions on FEL theory and Dr. John R. Harris for discussions on longitudinal beam dynamics. This work was performed under the auspices of the U.S. Department of Energy by the Lawrence Livermore National Laboratory under Contract No. DE-AC52-07NA27344.

[1] J. E. Walsh, in *Advances in Electronics and Electron Physics*, edited by C. Marton (Academic Press, New York, 1982), Vol. 58, p. 271.
[2] K. L. Felch, K. O. Busby, R. W. Layman, D. Kapilow, and J. E. Walsh, Appl. Phys. Lett. **38**, 601 (1981).
[3] E. P. Garate, S. Moustaizis, J. M. Buzzi, C. Rouille, H. Lamain, J. Walsh, and B. Johnson, Appl. Phys. Lett. **48**, 1326 (1986).
[4] H. Kosai, E. Garate, A. Fisher, and W. Main, IEEE Trans. Plasma Sci. **20**, 288 (1992).
[5] W. T. Main, E. Garate, J. C. Weatherall, and R. Cherry, IEEE Trans. Plasma Sci. **20**, 281 (1992).
[6] W. Peter, E. Garate, W. Main, and A. Fisher, Phys. Rev. Lett. **65**, 2989 (1990).
[7] S. M. Wiggins, D. A. Jaroszynski, B. W. J. McNeil, G. R. M. Robb, P. Aitken, A. D. R. Phelps, A. W. Cross, K. Ronald, N. S. Ginzburg, V. G. Shpak, M. I. Yalandin, S. A. Shunailov, and M. R. Ulmaskulov, Phys. Rev. Lett. **84**, 2393 (2000).
[8] L. Schächter, *Beam-Wave Interaction in Periodic and Quasi-Periodic Structures* (Springer, Berlin, 1997).
[9] M. Shoucri, Phys. Fluids **26**, 2271 (1983).
[10] G. Mishra and V. K. Tripathi, IEEE Trans. Plasma Sci. **17**, 12 (1989).
[11] S.-K. Kim, J.-S. Choi, and D.-I. Choi, IEEE Trans. Plasma Sci. **17**, 576 (1989).
[12] S.-F. R. Chang, J. E. Scharer, and J. H. Booske, IEEE Trans. Plasma Sci. **20**, 293 (1992).
[13] J. Joe, J. Scharer, J. Booske, and B. McVey, Phys. Plasmas **1**, 176 (1994).
[14] B. B. Godfrey, IEEE Trans. Plasma Sci. **7**, 53 (1979).
[15] D. S. Lemons and L. E. Thode, Phys. Rev. Lett. **56**, 2684 (1986).
[16] H. P. Freund, Phys. Rev. Lett. **65**, 2993 (1990).
[17] H. P. Freund and A. K. Ganguly, Phys. Fluids B **2**, 2506 (1990).
[18] T. D. Pointon and J. S. DeGroot, Phys. Fluids **31**, 908 (1988).
[19] J. C. Weatherall and W. Main, Phys. Fluids B **4**, 1953 (1992).
[20] S. A. Naqvi, J. A. Nation, L. Schächter, and Q. Wang, IEEE Trans. Plasma Sci. **26**, 840 (1998).
[21] N. S. Ginzburg, A. S. Sergeev, Yu. V. Novozhilova, I. V. Zotova, R. M. Rosenthal, A. D. R. Phelps, A. W. Cross, P. Aitken, V. G. Shpak, M. I. Yalandin, S. A. Shunailov, and M. R. Ulmaskulov, Opt. Commun. **175**, 139 (2000).
[22] D. A. Jaroszynski, S. M. Wiggins, B. W. J. McNeil, G. R. M. Robb, P. Aitken, A. D. R. Phelps, A. W. Cross, K. Ronald, V. G. Shpak, M. I. Yalandin, and N. S. Ginzburg, Nucl. Instrum. Methods Phys. Res., Sect. A **445**, 261 (2000).
[23] M. Abramowitz and I. A. Stegun, *Handbook of Mathematical Functions* (Dover, New York, 1964), 9th ed., Eq. 13.1.10.
[24] M. Abramowitz and I. A. Stegun, *Handbook of Mathematical Functions* (Dover, New York, 1964), 9th ed., Eq. 13.3.2.
[25] E. B. Manring, IEEE Microwave Guided Wave Lett. **3**, 78 (1993).
[26] L. Schächter, *Beam-Wave Interaction in Periodic and Quasi-Periodic Structures* (Springer, Berlin, 1997), p. 140.
[27] W. Case, in *High-Power Microwave Sources*, edited by V. L. Granatstein and I. Alexeff (Artech House, Boston, 1987), p. 405.
[28] LSP is a product of Voss Scientific, Albuquerque, New Mexico.
[29] J. M. Ortega, R. Prazeres, F. Glotin, and D. A. Jaroszynski, Phys. Rev. E **57**, 1053 (1998).